THE ASTROPHYSICAL JOURNAL, 505:999–1006, 1998 October 1

CORONAL COMPOSITION ABOVE THE SOLAR EQUATOR AND THE NORTH POLE AS DETERMINED FROM SPECTRA ACQUIRED BY THE SUMER INSTRUMENT ON *SOHO*

U. FELDMAN,[1] U. SCHÜHLE,[2] K. G. WIDING,[1] AND J. M. LAMING[3]

Received 1998 January 8; accepted 1998 April 30

ABSTRACT

Using spectra obtained by the SUMER instrument on the *Solar and Heliospheric Observatory* (*SOHO*) we have determined the composition of the bulk of the coronal plasma in the vicinity of the solar surface over a polar coronal hole and an equatorial region. Our measurements show that although low first ionization potential (FIP) elements are enriched by about a factor of 4 in the corona above the quiet equatorial region, little or no enrichment exists above the north polar coronal hole. These observations are in good agreement with the *Ulysses in situ* observations in both fast speed and slow speed winds.

Subject headings: Sun: abundances — Sun: corona

1. INTRODUCTION

Many solar wind composition studies have been done from spacecraft moving in the equatorial plane, which, therefore, primarily monitor the solar wind from equatorial regions of the sun. This low-latitude component of the solar wind is generally dominated by the slow-speed wind, which is highly variable with velocities generally less than 450 km s^{-1}. In describing the composition of the solar outer atmosphere, including the solar wind, it is convenient to introduce the concept of FIP bias. This refers to the result that elements with first ionization potential (FIP), less than about 10.5 eV, are found to be relatively more abundant (by a factor called the "FIP bias") than elements with high ionization potential, compared to the elemental distribution of the solar photosphere. In this context the composition of the slow-speed solar wind has been found to have a FIP bias of 4–5 (Bochsler & Geiss 1989; Gloeckler & Geiss 1989; von Steiger, Geiss, & Gloeckler 1997; Garrard & Stone 1993 from energetic particles). However, a second, more steady component of the solar wind with velocities in excess of 500 km s^{-1}, the fast-speed wind, is known to have a composition with a FIP bias of 2 or less (Gloeckler & Geiss 1989). During the *Skylab* mission in 1973–1974 the fast wind was shown to be correlated with coronal hole regions on the Sun and, therefore, with regions of open magnetic fields (Krieger, Timothy, & Roelof 1973; Nolte et al. 1975; von Steiger et al. 1997). This also implied that the slow-speed solar wind may originate from above closed field equatorial regions.

These characteristics of the solar wind have been confirmed and displayed in greater detail with observations from the *Ulysses* spacecraft. *Ulysses* contained particle-monitoring capabilities and was placed in an orbit inclined to the ecliptic in order to observe the solar wind from progressively higher solar latitudes. The observations showed a variable solar wind at lower latitudes giving way to a faster more steady wind reaching 750 km s^{-1} velocity at the south and north polar caps (Geiss et al. 1995; von Steiger et al. 1997). Associated with this was a change in the composition from a typical coronal FIP bias of 4–5 at low latitudes to a composition with a FIP bias approaching 1 in the fast wind from higher latitudes. This is best shown by a strong correlation between the stream velocity and the Mg/O abundance ratio (Geiss et al. 1995; von Steiger 1996). The fast-speed wind which has a typical FIP bias of 1.5 is associated with an O^{+7}/O^{+6} freeze-in temperature of 1.2×10^6 K (corresponding to a height of 1.3 $R_\odot$) in the model of the polar coronal hole given by Ko et al. (1997). The freeze-in temperatures refer to the coronal electron temperature at the altitude where the expansion time scale of the solar wind overcomes the collision and recombination time with the hot electrons, and the ionization state is "frozen-in" (von Steiger 1996). The low freeze-in temperature in the fast solar wind confirms its origin from the polar coronal hole. The O^{+7}/O^{+6} freeze-in temperature in the slow speed solar wind is higher and reaches a value of 1.6×10^6 K. Using the C^{+6}/C^{+5} freeze-in temperatures which are about 23% lower, the fast-speed wind temperature is 0.98×10^6 K and the slow-speed wind temperature is 1.3×10^6 K. The C^{+6}/C^{+5} fast-speed wind temperature of 0.98×10^6 K compares to a height near 1.2 $R_\odot$, in the south polar coronal hole model of Ko et al. (1997).

The solar wind abundance ratio of H/O has been studied extensively over several decades. Latest measurements indicate that in the slow-speed solar wind $H/O = 1890 \pm 600$ and in the high-speed solar wind $H/O = 1590 \pm 500$ (Wimmer Schweingruber 1994). Since the ratio of $H/O = 1175$ in the photosphere, the depletion in the solar wind of O when compared to the photosphere, if it exists at all, is 0.6 or less. For detailed accounts on solar wind observations see Bame et al. (1977), Gloeckler & Geiss (1989), Schwenn (1990), Meyer (1992), von Steiger et al. (1995), and von Steiger et al. (1997).

Spectroscopic instruments flown in the past were not designed to provide optimal observations for determining the coronal compositions above quiet and coronal hole regions. Thus, only little was known about the average plasma composition of these regions in the vicinity of the solar surface. The only exceptions were measurements done to determine the composition differences between polar and equatorial regions in the 4.3×10^5 K temperature range (Feldman & Widing 1993). This study made use of Ne VI and Mg VI limb-brightened emission rings near 400 Å surrounding the full-disk images in *Skylab* spectroheliograms

[1] E. O. Hulbert Center for Space Research, Mail Code 7608, Naval Research Laboratory, 4555 Overlook Avenue, SW, Washington, DC 20375.

[2] Max-Planck-Institut für Aeronomie, Max-Planck-Strasse 2, D-37191 Katlenburg-Lindau, Germany.

[3] SFA, Inc., 1401 McCormick Drive, Largo, MD 20774; and E. O. Hulbert Center for Space Research, Mail Code 7608, Naval Research Laboratory, 4555 Overlook Avenue, SW, Washington, DC 20375.

(Tousey et al. 1977). The relative intensities of the sharp emission rings were used like the intensities from a slit spectrum to compare the abundance of the low-FIP Mg with the abundance of the high-FIP Ne. In particular, the intensity ratios of (Mg VI-400.68)/(Ne VI-401.14) and of (Mg VI-400.68)/(Ne VI-401.94) limb-brightened rings were used to determine the Mg/Ne abundance ratios above polar coronal holes and above a quiet region. Postulating that Mg and Ne are good representatives of low- and high-FIP elements their abundance ratio was used as a measure of the FIP bias. Measurements of the rings above the polar coronal hole showed enrichment of Mg when compared to Ne with a FIP bias less than or equal to 2.5. In the bright rings over the quiet limb the FIP bias was found to be less than or equal to 2. In the quiet-limb region just outside the coronal hole boundaries the composition was found to be nearly photospheric. The findings show that the 4.3×10^5 K plasma composition above coronal hole and quiet-Sun regions does not agree with compositions of the slow and the fast-speed winds observed by *Ulysses*. As suggested by Feldman & Widing (1993), the difference may mean that the unresolved fine structures (UFS) forming the Ne VI and Mg VI emission rings are not the dominant source of the solar wind which may rather be correlated with the mostly open-field magnetic region surrounding the UFS.

The composition of equatorial coronal streamers at a distance of 1.5 $R_\odot$ above a quiet and an active region was recently studied using measurements obtained from the UVCS instrument on *SOHO* (Raymond et al. 1997). In general, they found that the enrichment of the low-FIP elements are consistent with values seen in the slow-speed wind. The measurement at the limb of the streamer nicely confirms that the slow wind flows around the streamer as predicted by von Steiger et al. (1995). However, by using the intensity ratios of the high FIP O VI resonance line and the H Lβ line they found that oxygen is depleted at 1.5 $R_\odot$ by as much as 1 order of magnitude when compared with photospheric abundances. This result is in contradiction to H/O ratios derived from measurements of the slow-speed or the fast-speed solar wind.

The aim of the present work is to determine the composition of the bulk of the coronal plasma in the vicinity of the solar surface over a polar hole and an equatorial region. We compare our measurements, which were recorded close to the solar limb ($h \leq 1.03\ R_\odot$) with the UVCS streamer taken at 1.5 $R_\odot$, and the *Ulysses* measurements of the slow-speed solar wind in the equatorial plane and the fast-speed solar wind along the polar direction.

2. OBSERVATIONS AND DATA REDUCTIONS

The SUMER instrument is a high spectral and spatial resolution slit spectrometer accommodated on *SOHO*. The wavelength range for the detector used to obtain the present observations (detector B) is 660–1500 Å in first order and 500–750 Å in second order. The instrument radiometric efficiency has been calibrated before and during the flight. It is fairly constant over the 900–1200 Å range; however, outside this range it varies considerably. The spatial resolution along the length of the slit is about 1″ and the spectral resolution is about 43 and 22 mÅ in first and second orders, respectively. The instrument is described in detail by Wilhelm et al. (1995) and Wilhelm et al. (1997). A common SUMER data acquisition mode is the "reference spectrum" where the entire wavelength range is covered by some 60 spectral images. In a reference spectrum mode each of the images is shifted by $\sim$13 Å (in first order) from the previous image. For our study we have selected two sets of data recorded in the reference spectrum mode. In both cases a 4×300 arcsec^2 slit and a 300 s integration time were used to acquire each image, i.e., a full reference spectrum was acquired in $\sim$5 h. The elemental composition of the corona above the polar coronal hole was deduced from a reference spectrum that was acquired on 1996 November 3. During the exposures, the slit was oriented in the north-south direction. The slit's lower edge was aligned to record spectra emitted from a region 22″ above the north polar limb. The elemental compositon of the corona above a quiet equatorial region was acquired on 1996 November 21 and 22. At that time *SOHO* underwent a 90° roll maneuver, and the SUMER entrance slit was oriented on the solar equator along the east-west direction. The slit's lower edge imaged coronal plasma that was located 24″ above the limb. During the time of the observations the corona along the entire equatorial region was very quiet. For details see the 10^6 K solar image of Figure 1 that was exposed on 1996 November 22 by EIT on *SOHO*.

Prior to obtaining the line intensities, the raw spectral images were corrected for flat-field and image distortion effects using standard SUMER programs. Sets of highly ionized lines, one from high-FIP elements and a second from low-FIP elements, were selected for analysis. The lines used for studying the corona above the polar coronal hole are listed in column (1) of Tables 1 and 2, and those selected for studying the quiet corona above the equatorial region are listed in the first column of Tables 3 and 4. For each line the counts accumulated over the entire line width ($\Delta\lambda$) were integrated. Similarly, we have integrated the counts over a $\Delta\lambda$ width in an adjacent region devoid of spectral lines. The net counts, which is the difference between the two measurements, obtained through the lower edge of the slit are given in column (2) of the tables. Line intensities have been deduced using the radiometric calibration curves of SUMER with the B-detector. Ratios between the instrument efficiency at 1032 Å (O VI) and at the wavelength of the

TABLE 1

HIGH-FIP LINES IN THE CORONA ABOVE A POLAR CORONAL HOLE REGION

			EMISSIVITY			
λ (1)	COUNTS (2)	EFFICIENCY (3)	log $T_e = 5.8$ (4)	log $T_e = 5.9$ (5)	log $T_e = 6.0$ (6)	log $T_e = 6.1$ (7)
O VI λ1032	58000	1.0	2.57−13	1.19−13	6.72−14	4.52−14
Ne VII λ895	1400	1.13	2.11−14	3.22−15	4.59−16	8.12−17
Ne VIII λ780......	5000	2.70	1.68−13	8.78−14	3.72−14	1.67−14
S IX λ871	75	1.30	5.90−17	2.53−16	3.56−16	1.94−16

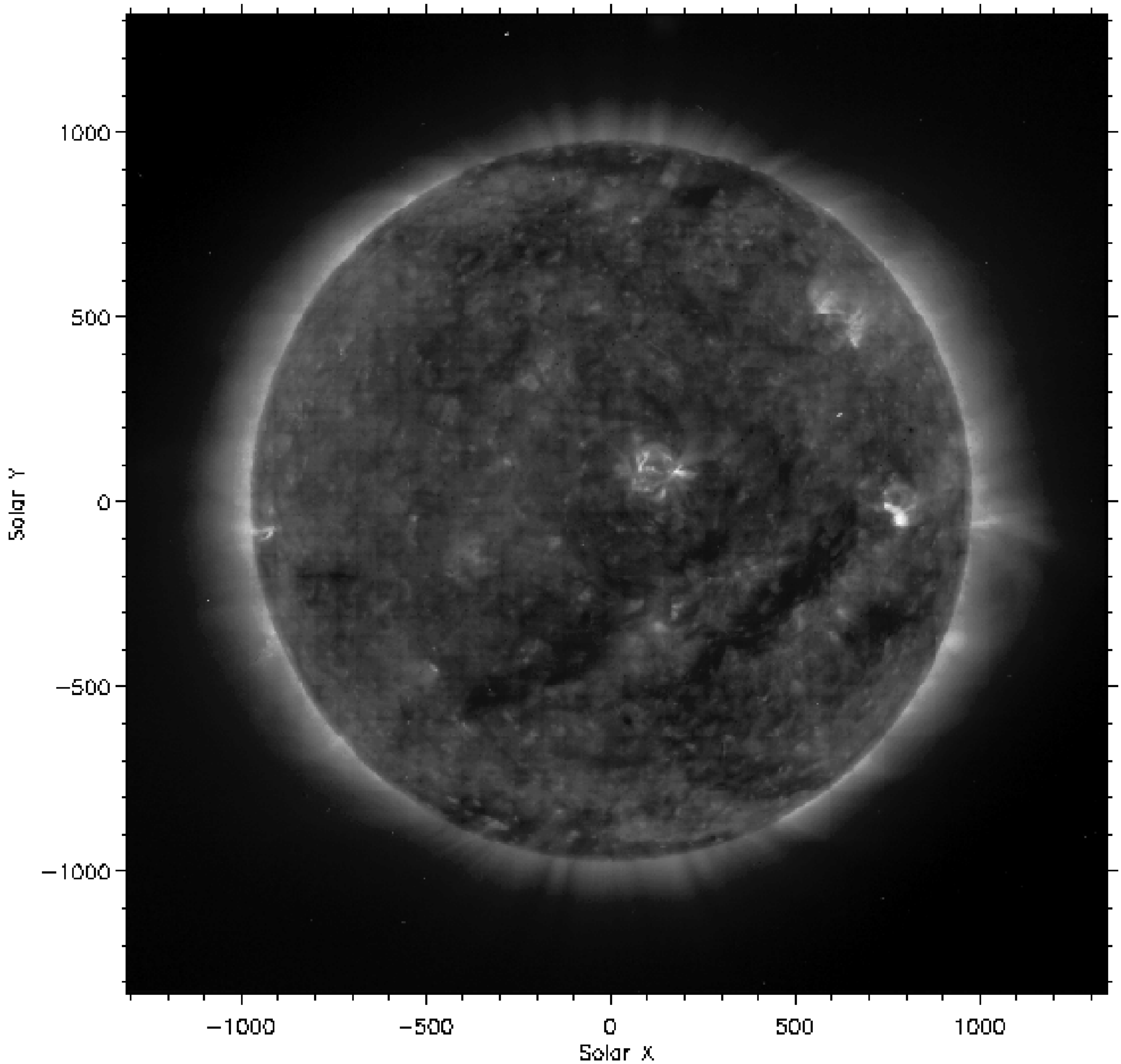

FIG. 1.—EIT image of the 1×10^6 K solar corona taken at 171 Å. Transitions of Fe IX and Fe X are the most prominent contributors to the detected emission.

lines under consideration are given in column (3) of each table.

Theoretical emissivities for all the lines were obtained from calculations or compilations done by either Raymond et al. (1997) or by us. We have used statistical equilibrium model ions, generally including 15–20 levels. Electron impact collision strengths or excitation rates come from various sources in the literature. These are either ***R***-matrix calculations including resonances or distorted wave results that generally omit the effects of resonances in excitation cross sections. In the latter case we have included an estimate of the resonance contribution using the HULLAC suite of codes (Klapisch et al. 1988) as described for the N-like system in Laming et al. (1997). Where they are appropriate, proton impact excitation rates have also been included between fine-structure levels.

In detail, Raymond et al. (1997) compiled the atomic data for H from Scholz & Waters (1991), Callaway & McDowell (1983), and Hummer (1994). Atomic data for ions in the Be-, B-, and N-like systems are identical to those used in Laming et al. (1997). Collision strengths for N V are from Merts et al. (1980) and for O VI are from Zhang, Sampson, & Fontes (1990). Data for the rest of the Li-like ions is taken purely from HULLAC computations for $n = 2$ and $n = 3$ levels. The distorted wave approximation should be perfectly adequate for the $2s$–$2p$ resonance transitions we observe. Data for the C-like ion Mg VII are taken from Mason & Bhatia (1978), for both electron impact excitation and radiative

TABLE 2

LOW-FIP LINES IN THE CORONA ABOVE A POLAR CORONAL HOLE

λ (Å) (1)	COUNTS (2)	EFFICIENCY (3)	EMISSIVITY log $T_e = 5.8$ (4)	log $T_e = 5.9$ (5)	log $T_e = 6.0$ (6)	log $T_e = 6.1$ (7)
O VI λ1032	58000	1.00	2.57−13	1.19−13	6.72−14	4.52−14
Na IX λ681	420	4.6	1.03−15	4.18−15	3.09−15	1.43−15
Mg VII λ868	480	1.3	2.48−15	1.14−15	1.60−16	4.65−18
Mg VIII λ782......	320	2.7	1.15−15	1.98−15	9.67−16	1.00−16
Mg X λ609........	2400	3.3	2.01−16	6.93−15	4.28−14	4.05−14
Si VII λ1049.......	300	1.0	1.60−15	6.99−16	1.52−16	1.81−17
Si VIII λ949	870	1.05	1.42−15	2.08−15	1.31−15	3.84−16
Si IX λ950.........	350	1.05	7.18−17	3.88−16	6.96−16	4.70−16
Ca X λ557	220	6.75	4.31−15	2.86−15	1.42−15	7.06−16
Fe X λ1028	350	1.00	1.87−16	5.97−16	8.89−16	4.55−16

decay rates. Proton impact excitation rates are taken from Faucher, Masnon-Seeuws, & Prudhomme (1980) for the ground ^3P term, and calculated by us for the $^1D_2$–$^1S_0$ transition. The contributions of resonances to transitions between different levels of the ground configuration are calculated as outlined in Laming et al. (1997). At temperatures lower than those corresponding to collisional ionization equilibrium for Mg^{6+}, good agreement is found between our procedure and the ***R***-matrix results of Lennon & Burke (1994), adding to our confidence in applying this correction. Si IX is taken from Zhang & Sampson (1996). The O-like ions Si VII and S IX are taken from Lang & Summers (1994), who tabulate electron impact excitation rates as a function of temperature calculated from the cross sections of Bhatia, Feldman, & Doschek (1979). Radiative decay rates are also taken from this last reference. Proton and resonance rates are calculated by us as described for other isoelectronic sequences. The remaining ions Fe X and Fe XII are taken from Bhatia & Doschek (1995) and Tayal & Henry (1988). The Fe X data are calculated in the distorted wave approximation but appear to be more reliable than more recent close-coupling results (see discussion in Laming 1998, and references therein).

The emission rates per ion calculated above are multiplied by the ionization fraction and by the photospheric element abundance to give an emission rate per unit electron density (n_e), per unit proton density (n_p), and per unit volume (cm^{-3}), assuming H to be fully ionized. Ionization fractions for all elements but Fe are taken from Arnaud & Rothenflug (1985) and for Fe from Arnaud & Raymond

TABLE 3

HIGH-FIP LINES IN THE CORONA ABOVE AN EQUATORIAL QUIET REGION

λ (Å) (1)	COUNTS (2)	EFFICIENCY (3)	EMISSIVITY log $T_e = 6.0$ (4)	log $T_e = 6.1$ (5)	log $T_e = 6.2$ (6)	log $T_e = 6.3$ (7)
Lyβ λ1025........	980	1.0	1.31−15	1.04−15	7.47−16	2.59−16
O VI λ1032	34000	1.0	6.72−14	4.52−14	3.17−14	1.85−14
N V λ1238........	1300	1.4	3.52−14	2.24−15	1.07−15	3.54−16
S X λ1196	900	1.1	...	9.83−16	7.66−15	2.63−16
S X λ1213	2000	1.2	...	2.18−15	1.66−15	4.46−16
Ne VII λ895	60	1.13	4.59−16	8.12−17	1.88−17	5.45−18
Ne VIII λ780......	2800	2.70	3.72−14	1.67−14	8.80−15	5.55−15
S IX λ871	180	1.30	3.56−16	1.94−16	5.22−17	7.00−18

TABLE 4

LOW-FIP LINES IN THE CORONA ABOVE AN EQUATORIAL QUIET REGION

λ (Å) (1)	COUNTS (2)	EFFICIENCY (3)	EMISSIVITY log $T_e = 6.0$ (4)	log $T_e = 6.1$ (5)	log $T_e = 6.2$ (6)	log $T_e = 6.3$ (7)
O VI λ1032	34000	1.0	6.72−14	4.52−14	3.17−14	1.85−14
Na IX λ681	620	4.6	3.09−15	1.43−15	6.54−16	3.44−16
Mg VIII λ782......	60	2.7	9.67−14	1.00−16	7.01−18	6.39−19
Mg X λ609........	20000	3.3	4.28−14	4.05−14	1.95−14	8.96−15
Si VIII λ949	480	1.05	1.31−15	3.84−16	4.50−17	1.67−18
Si IX λ950.........	1000	1.05	6.96−15	4.70−16	1.06−16	6.75−18
Ca X λ557	350	6.75	1.42−15	7.06−16	2.69−16	6.11−17
Fe X λ1028	800	1.0	8.89−16	4.55−16	8.07−17	8.90−18
Fe XII λ1242	7000	1.4		4.37−15	2.92−15	5.01−16

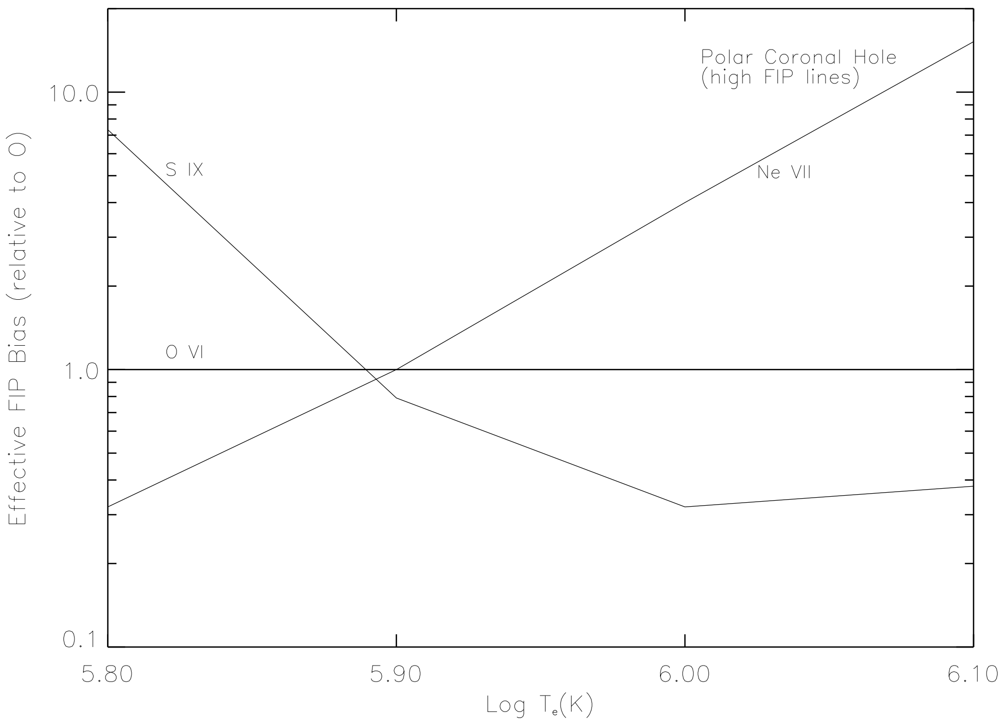

FIG. 2*a*

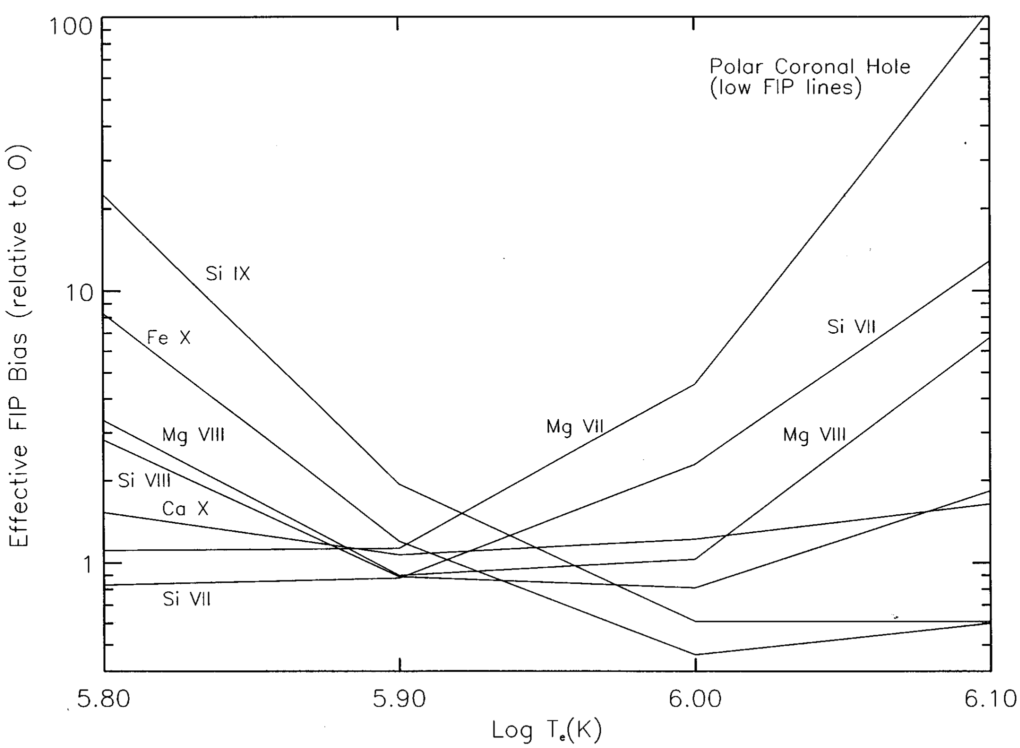

FIG. 2*b*

FIG. 2.—Plot of the effective FIP bias as a function of temperature for the corona above the polar coronal hole. (*a*) High-FIP lines; (*b*) low-FIP lines. Li-Like Ne VIII, Na IX, and Mg X lines are not shown.

(1992). Photospheric abundances are taken from Feldman (1992), which are based on Anders & Grevesse (1989). An electron density of 1×10^8 cm^{-3} was used in calculating the emissivities of the corona above the polar coronal hole. For the quiet corona an electron density of 2×10^8 cm^{-3} was used. Electron densities for the coronal regions we have considered were determined from the 1445 Å/1440 Å Si VIII line ratios. (For details on the technique see Feldman et al. 1978 and Laming et al. 1997). Columns (4), (5), (6), and (7) in the tables provide the calculated emissivities for each of four

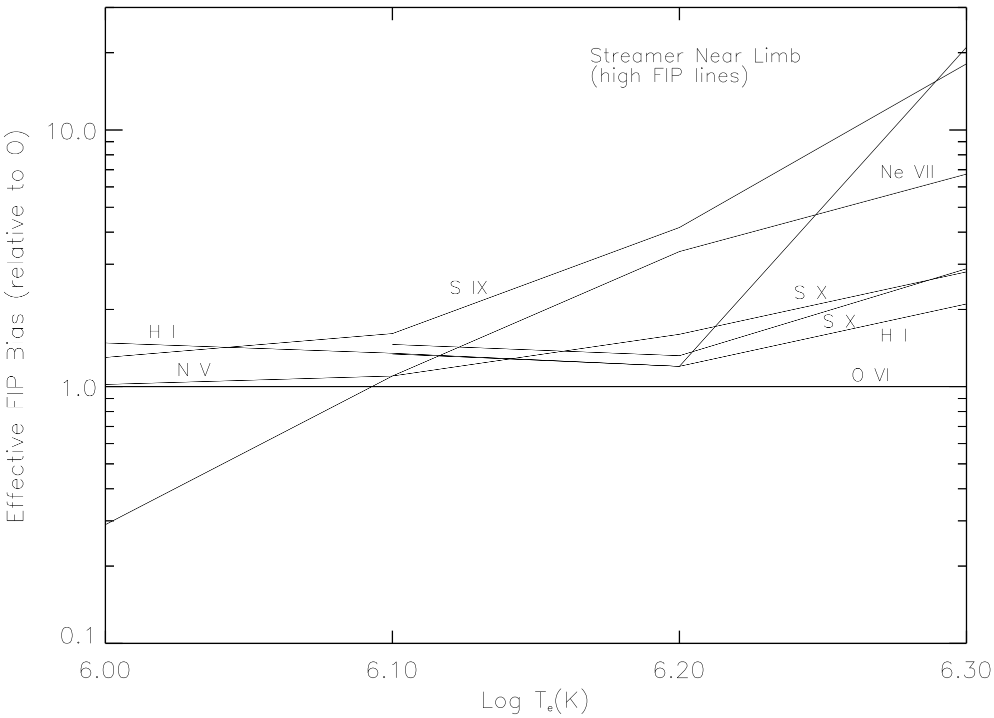

FIG. 3*a*

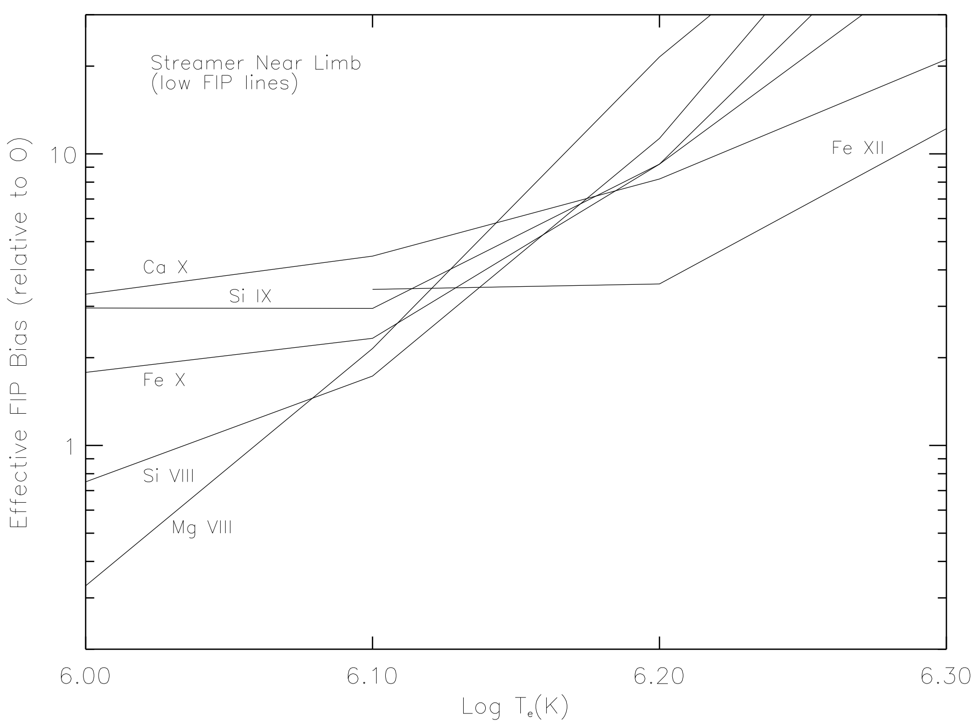

FIG. 3*b*

FIG. 3.—Plot of the effective FIP bias as a function of temperature for the corona above the quiet equatorial region. (*a*) High-FIP lines; and (*b*) low-FIP lines. Li-like Ne VIII, Na IX, and Mg X lines are not shown.

different temperatures.

We initially tried to derive an emission measure distribution for both the coronal hole and streamer data sets, using the methods described by Laming, Drake, & Widing (1996). We assume that the plasma emission measure is distributed over a range of temperatures and attempt to find it by iterating an initial guess at the emission measure distribution until the observed line intensities are reproduced. Unlike that work, where the emission measure converged quite quickly to a stable distribution, we found a stable physically plausible result rather hard to find. In general, our emission distributions eventually collapsed to a single temperature. Often such a behavior is the result of the ill-conditioned nature of such inversion problems; however, in these cases it appears that we are observing essentially isothermal plasmas. In studying the streamer at 1.5 $R_{\odot}$, Raymond et al. (1997) also found that an isothermal temperature of 1.58×10^6 K (log $T_e = 6.2$) is the best representation for the plasma they studied. Therefore, we too make this assumption and derive "tentative coronal elemental enrichment values" (effective FIP bias values) for the four temperatures using the following relationship. We first assumed that oxygen is a proper high-FIP element to which the abundance of all other elements can be normalized. Second, we normalized with respect to the 1032 Å O VI line the measured count rates as well as the calculated emissivitites of all other lines. The effective FIP bias versus temperature we derived is the ratio of the above two ratios, i.e.,

$$\text{effective FIP bias } \{T_e\} = \frac{[(\text{Corrected count in line})/(\text{count in O VI})]}{[(\text{emissivity in line})/(\text{emissivity in O VI})]\{T_e\}} .$$

The last four columns in each table provide the effective FIP bias $\{T_e\}$. Figures 2*a* and 2*b* are plots of the effective FIP bias as a function of temperature for the corona above the polar coronal hole, and Figures 3*a* and 3*b* provide similar results for the quiet corona. For reasons that are not clear to us, the Ne VIII, Na IX, and Mg X lines, all of which belong to the Li-like isoelectronic sequence, appear to indicate a systematic lower effective FIP bias value than the rest of the lines. To avoid confusion we did not plot them in these figures; however, we have plotted them in a later display.

3. DISCUSSION AND CONCLUSION

3.1. *FIP Bias in the Corona above the Solar Pole*

As seen from Figures 2*a* and 2*b*, the effective FIP bias of most lines intersect each other at a temperature of log $T_e = 5.92$ ($T_e = 8.3 \times 10^5$ K). Accepting $T_e = 8.3 \times 10^5$ K as the plasma temperature of the corona above the polar coronal hole, the FIP bias value for each of the lines is plotted in Figure 4. The Li-Like Ne VIII, Na IX, and Mg X lines are represented in the figure with open circles, while the rest are represented using full circles. As seen from the figure, the FIP bias in the corona above the coronal hole is very close to 1. It appears that the coronal plasma did not undergo any composition modification after emerging from under the photosphere. The south polar coronal hole model of Ko et al. (1997) predicts that the freeze-in temperature ($T_e = 1.2 \times 10^6$ K) of the fast-speed solar wind occurs at a height of 1.3 $R_{\odot}$. Since the spectroscopic measurements of the polar coronal hole composition reported here refers to a much lower coronal altitude ($h < 1.03$ $R_{\odot}$), it is not surprising that a lower temperature ($T_e = 8.3 \times 10^5$ K) is derived.

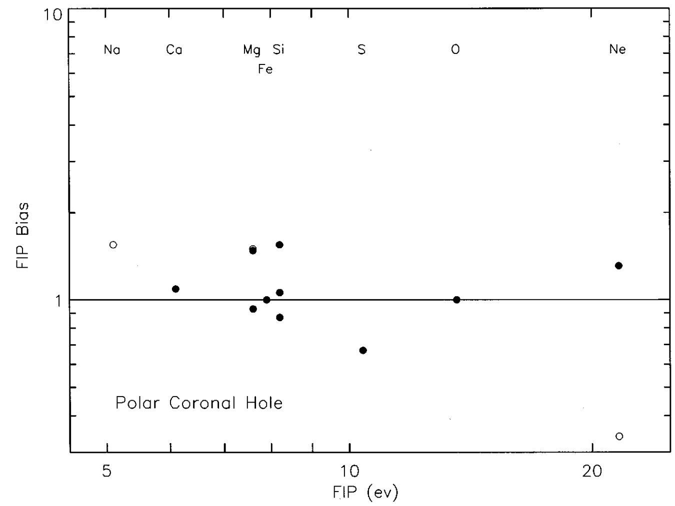

FIG. 4.—FIP bias vs. FIP for the corona above the polar coronal hole. Li-like Ne VIII, Na IX, and Mg X lines are represented with open circles.

3.2. *FIP Bias in the Corona along the Equatorial Plane*

Figures 3*a* and 3*b* show that both the high- and low-FIP lines intersect each other at a temperature of log $T_e = 6.13$ ($T_e = 1.35 \times 10^6$ K): the high-FIP lines cross each other at a FIP value of slightly above 1, while the low-FIP lines cross at a value which is closer to 3 or 4. The Li-like Ne VIII, Na IX, and Mg X lines are represented in the figures with open circles, while the rest are represented using full circles. Accepting $T_e = 1.35 \times 10^6$ K as the plasma temperature of the corona in the equatorial direction above the quiet limb, the FIP bias value for each of the lines is plotted in Figure 5. As can be seen from the figure, all high-FIP elements including H have a FIP bias of 1, while the low-FIP elements have a FIP bias value of about 4. The spectroscopic measurements above the quiet region refers to a fairly low coronal altitude ($h < 1.03$ $R_{\odot}$), while the freeze-in temperature most likely occurs at much higher coronal heights. It is, therefore, not surprising that the spectroscopic determined temperature is some 15% lower than the freeze-in temperature measured from the O^{+7}/O^{+6} ions ratios.

Again, although the coronal temperature above the equatorial quiet region determined by spectroscopic means is 15% lower than the slow-speed solar wind value ($T_e = 1.6 \times 10^6$ K) obtained from the O^{7+}/O^{6+} freeze-in

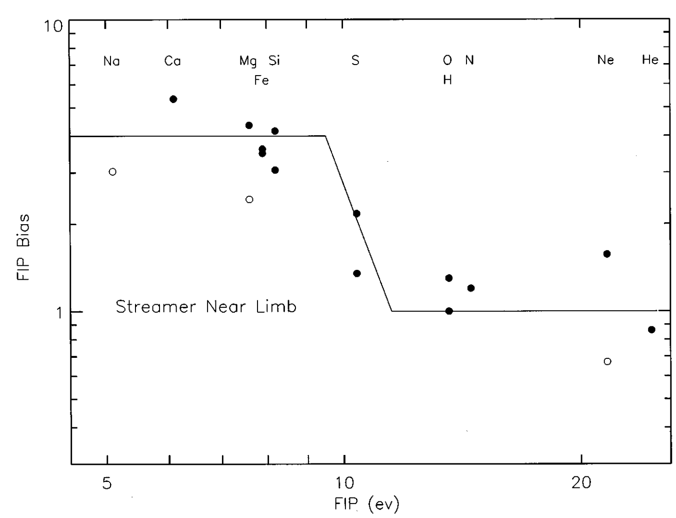

FIG. 5.—FIP bias vs. FIP for the corona above the quiet equatorial region. Li-like Ne VIII, Na IX, and Mg X lines are represented with open circles.

ratio, the C^{6+}/C^{5+} freeze-in value ($T_e = 1.3 \times 10^6$ K) is similar.

3.3. H/O *Abundance Ratio in the Equatorial Plane*

The H to O abundance ratio that we have obtained from the spectroscopic measurements above the equatorial region is H/O = 1500 $\pm$ 400. This result falls within the limits of the present measurements and theoretical calculation uncertainties of the slow-speed solar wind values. In contrast, the result is markedly different from the results reported by Raymond et al. (1997). In discussing their H/O abundance results, Raymond et al. (1997) suggested that elemental settling may be in part responsible for the large depletion of O they detected at a height of 1.5 $R_\odot$. Our observations confirm that the large depletion of O when compared with the much lighter H, which was detected by Raymond et al. (1997), is due to elemental settling. To prove that indeed elemental settling occurs at large coronal heights we display in Figure 6 the intensity versus height above the limb of Ne VIII, Mg X, Si XI, Si XII, Fe X, and Fe XII. The displayed intensities are taken from the set of spectral images that were also used to derive the composition of the quiet Sun. Notice that the intensity falloff of the Ne, Mg, and Si lines which have about the same mass is quite similar; however, the falloff of the twice heavier Fe is much faster. At about 400″ above the limb ($\sim 1.4\ R_\odot$) the Fe intensity has already fallen by about a factor of 2.

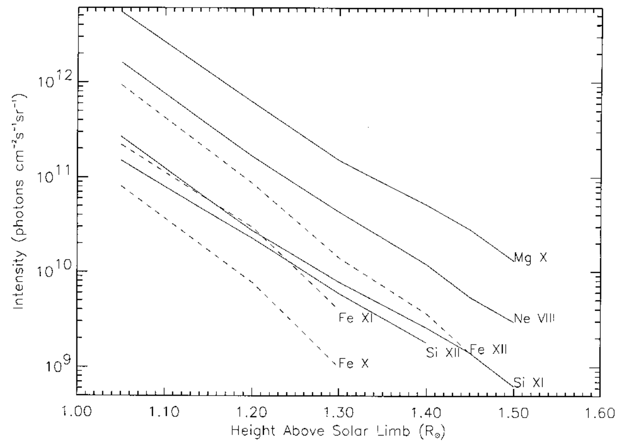

FIG. 6.—Relative line intensities as a function of height above the quiet equatorial region of a number of prominent spectral lines. Ne VIII 770.41 Å ($2s\,^2S_{1/2}$–$2p\,^2P_{3/2}$), Mg X 609.78 Å ($2s\,^2S_{1/2}$–$2p\,^2P_{3/2}$), Si IX 580.85 Å ($2s^2\,^1S_0$–$2s2p\,^3P_1$), and Si XII 499.40 Å ($2s\,^2S_{1/2}$–$2p\,^2P_{3/2}$) are plotted as solid curves. Fe X 1028.02 Å ($3p^4 3d\,^4D_{7/2}$–$3p^4 3d\,^4F_{7/2}$), Fe XI 1467.06 Å ($3p^4\,^3P_1$–$3p^4\,^1S_0$) and Fe XII 1242.00 Å ($3s^2 3p^3\,^4S_{3/2}$–$3s^2 3p^3\,^2P_{3/2}$) are plotted as dashed curves.

We would like to thank John Raymond for providing us with atomic data compilations of some of the solar abundant elements. We would also like to thank Catherine Abbott for her help in reducing the SUMER spectra. The comments by the anonymous referee, which helped to clarify a number of issues, are greatly appreciated. The Naval Research Laboratory contribution to this work was supported by the Office of Naval Research. The SUMER project is financially supported by DLR, CNES, NASA, and the ESA PRODEX program (Swiss contribution).

REFERENCES

Anders, E., & Grevesse, N. 1989, Geochim. Cosmochim. Acta., 53, 197
Arnaud, M., & Raymond, J. C. 1992, ApJ, 398, 394
Arnaud, M., & Rothenflug, R. 1985, A&AS, 60, 425
Bame, S. J., Asbridge, J. R., Feldman, W. C., & Gosling, J. T. 1977, J. Geophys. Res., 82, 1487
Bhatia, A. K., & Doschek, G. A. 1995, Atomic Data and Nuclear Data Tables, 60, 97
Bhatia, A. K., Feldman, U., & Doschek, G. A. 1979, A&A, 80, 22
Bochsler, F., & Geiss, J. 1989, in Solar System Plasma Physics, ed. J. H. Waite, Jr., J. L. Burch, & R. L. Moore, Geophys. Monogr., 54, 133
Callaway, J., & McDowell, M. R. C. 1983, Commun. Atom. Phys., 13, 19
Faucher, P., Masnou-Seeuws, F., & Prudhomme, M. 1980, A&A, 81, 137
Feldman, U. 1992, Phys. Scripta, 46, 202
Feldman, U., Doschek, G. A., Mariska, J. T., Bhatia, A. K., & Mason, H. E. 1978, ApJ, 226, 674
Feldman, U., & Widing, K. G. 1993, ApJ, 414, 381
Garrard, T. L., & Stone, E. C. 1993, in Proc. 23rd Int. Cosmic Ray Conf. (Calgary) 3, 384
Geiss, J. 1982, Space Sci. Rev., 33, 201
Gloeckler, G., & Geiss, J. 1989, in AIP Conf. Proc. 183, ed. C. J. Waddington (New York: AIP), 49
Geiss, J., et al. 1995, Science, 268, 1303
Hummer, D. G. 1994, MNRS, 268, 109
Ko, Y.-K., Fisk, L. A., Geiss, J., Gloeckler, G., & Guhathakurta, M. 1997, Sol. Phys., 171, 345
Klapisch, M., Bar Shalom, A., Goldstein, W. H., Meroz, E., Chon, A., & Cohen, M. 1988, HULLAC Code for Atomic Physics
Krieger, A. S., Timothy, A. F., & Roelof, E. C. 1973, Sol. Phys., 29, 505
Laming, J. M. 1998, in ASP Conf. Ser. 154, 10th Cambridge Workshop on Cool Stars, Stellar Systems, and the Sun, ed. J. A. Bookbinder & R. A. Donahue (San Francisco: ASP), 447
Laming, J. M., Drake, J. J., & Widing, K. G. 1996, ApJ, 462, 948
Laming, J. M., Feldman, U., Schühle, U., Lemaire, P., Curdt, W., & Wilhelm, K. 1997, ApJ, 485, 911
Lang, J., & Summers, H. P. 1994, At. Data. Nucl. Data Tables, 57, 215
Lennon, D. J., & Burke, V. M. 1994, A&AS, 103, 273
Mason, H. E., & Bhatia, A. K. 1978, MNRAS, 184, 423
Merts, A. L., Mann, J. B., Robb, W. D., & Magee, N. H., Jr. 1980, Los Alamos Informal Report LA-8267
Meyer, J. P. 1992, in Origin and Evolution of the Elements, ed. N. Prantzos, E. Vangioni-Flam, & M. Casse (Cambridge: Cambridge Univ. Press), 26
Nolte, J. T., Krieger, A. S., Timothy, A. F., Vaiana, C. S., & Zombeck, M. V. 1975, Sol. Phys., 46, 291
Raymond, J. C., et al. 1997, Sol. Phys., 175, 645
Scholtz, T. T., & Walters, H. R. 1991, ApJS, 380, 302
Schwenn, R. 1990, in Physics of the Inner Heliosphere, Vol. 1, ed. R. Schwenn & E. Marsch (Berlin: Springer-Verlag), 99
Tayal, S. S., & Henry, R. J. W. 1988, ApJ, 329, 1023
Tousey, R., Bartoe, J.-D. F., Brueckner, G. E., & Purcell, J. D. 1977, Appl. Opt., 16, 870
von Steiger, R., Wimmer Schweingruber, R. F., Geiss, J., & Gloeckler, G. 1995, Adv. Space Res., 15, (7) 3
von Steiger, R. 1996, in ASP Conf. Proc. 109, Cool Star, Stellar Systems, and the Sun, ed. R. Pallavicini & A. K. Dupree (San Francisco: ASP), 491
von Steiger, R., Geiss, J., & Gloeckler, G. 1997, in Cosmic Winds and the Heliosphere, ed. J. R. Jokipii, C. P. Sonett, & M. S. Giampapa (Tucson: Univ. Arizona Press), 581
Wilhelm, K., et al. 1995, Sol. Phys., 162, 189
Wilhelm, K., Lemaire, P., Feldman, U., Hollandt, J., Schühle, U., & Curdt, W. 1997, Appl. Opt., 36, 6416
Wimmer Schweingruber, R. F. 1994, Ph.D. thesis, Univ. Bern
Zhang, H. L., & Sampson, D. H. 1996, At. Data Nucl. Data Tables, 63, 275
Zhang, H. L., Sampson, D. H., & Fontes, C. J. 1990, At. Data Nucl. Data Tables, 44, 31